



**HAL**  
open science

## Effect of Pressure on Interband and Intraband Transition of Mercury Chalcogenides Quantum Dots

Clément Livache, Nicolas Goubet, Charlie Gréboval, Bertille Martinez, Julien Ramade, Junling Qu, Amaury Triboulin, Hervé Cruguel, Benoit Baptiste, Stefan Klotz, et al.

► **To cite this version:**

Clément Livache, Nicolas Goubet, Charlie Gréboval, Bertille Martinez, Julien Ramade, et al.. Effect of Pressure on Interband and Intraband Transition of Mercury Chalcogenides Quantum Dots. *Journal of Physical Chemistry C*, 2019, 10.1021/acs.jpcc.9b01695 . hal-02120607

**HAL Id: hal-02120607**

**<https://hal.science/hal-02120607v1>**

Submitted on 30 Oct 2019

**HAL** is a multi-disciplinary open access archive for the deposit and dissemination of scientific research documents, whether they are published or not. The documents may come from teaching and research institutions in France or abroad, or from public or private research centers.

L'archive ouverte pluridisciplinaire **HAL**, est destinée au dépôt et à la diffusion de documents scientifiques de niveau recherche, publiés ou non, émanant des établissements d'enseignement et de recherche français ou étrangers, des laboratoires publics ou privés.

# Effect of Pressure on Interband and Intraband Transition of Mercury Chalcogenides Quantum Dots

Clément Livache<sup>1,2</sup>, Nicolas Goubet<sup>1,2</sup>, Charlie Gréboval<sup>1</sup>, Bertille Martinez<sup>1,2</sup>, Julien Ramade<sup>1</sup>, Junling Qu<sup>1</sup>, Amaury Triboulin<sup>1</sup>, Hervé Cruguel<sup>1</sup>, Benoit Baptiste<sup>3</sup>, Stefan Klotz<sup>3</sup>, Guy Fishman<sup>4</sup>, Sébastien Sauvage<sup>4</sup>, Francesco Capitani<sup>5</sup>, Emmanuel Lhuillier<sup>1\*</sup>

<sup>1</sup>Sorbonne Université, CNRS, Institut des NanoSciences de Paris, INSP, F-75005 Paris, France

<sup>2</sup>Laboratoire de Physique et d'Etude des Matériaux, ESPCI-ParisTech, PSL Research University, Sorbonne Université UPMC Univ Paris 06, CNRS, 10 rue Vauquelin 75005 Paris, France.

<sup>3</sup>Sorbonne Université, CNRS, Institut de Minéralogie, de Physique des Matériaux et de Cosmochimie, IMPMC, F-75005 Paris, France

<sup>4</sup>Centre de Nanosciences et de Nanotechnologies, CNRS, Univ. Paris-Sud, Université Paris-Saclay, C2N – 10 boulevard Thomas Gobert, 91460 Palaiseau, France

<sup>5</sup>Synchrotron-SOLEIL, Saint-Aubin, BP48, F91192 Gif sur Yvette Cedex, France

**Abstract:** Mercury chalcogenide nanocrystals generate a lot of interest as active materials for low cost infrared sensing. Device improvement requires building a deeper understanding of their electronic structure which combines inverted band ordering, quantum confinement and dependence to surface chemistry. This is particularly true with the development of mercury chalcogenide colloidal heterostructures (HgSe/HgTe, HgTe/CdS...). In this case the lattice mismatch induces a strain which affects significantly the band gap given the narrow band gap nature of the material. Here we study the effect of pressure on interband and intraband transitions in a series of HgTe and HgSe colloidal quantum dots. We demonstrate that in HgTe and HgSe, the nanocrystal morphology stabilizes the zinc blende phase up to 3 GPa. Under compressive strain, the interband signal blueshifts by 60 meV/GPa, while the intraband transition redshifts by a small amount (8 meV/GPa). Using an 8-band k-p formalism, we reveal that the interband shift has the same origin as the one observed for bulk material (change of effective mass, followed by band gap opening), while the intraband shift can be attributed to an increase of effective mass only.

\*To whom correspondence should be sent: [el@insp.upmc.fr](mailto:el@insp.upmc.fr)

## INTRODUCTION

Mercury chalcogenides (HgX) colloidal quantum dots (CQDs) are promising emerging technology for the design of low cost infrared devices such as detectors<sup>1-6</sup> and low threshold lasers.<sup>7</sup> Interest for these materials under colloidal form is also driven by more fundamental effects such as multi exciton generation,<sup>8,9</sup> and possible emergence of topological effects.<sup>10</sup>

Among HgX, HgSe and HgTe are semimetals under bulk form.<sup>11</sup> Once confinement is added through the generation of quantum dot shape, HgSe and HgTe behave respectively as a degenerately n-doped semiconductor<sup>12-14</sup> and a narrow band gap intrinsic semiconductor with interband optical feature,<sup>15,16</sup> at least in the range of CQD sizes of interest in this paper. As a result, these materials are interesting platforms to investigate the physics of small energy transitions: interband transitions between two bands of a  $\Gamma_8$  geometry in the case of HgTe, and intraband transitions in the upper  $\Gamma_8$  band in the case of HgSe.<sup>17,18</sup>

Although the electronic structure of HgX nanocrystals<sup>19</sup> and their superlattices<sup>10</sup> has generated some interest recently, the effect of pressure on HgX confined nanoparticles remains currently uninvestigated. This question is nevertheless of great interest, especially for the study of HgX nanocrystal based heterostructures and their strained interfaces. Recently, it was proposed by Goubet *et al.*<sup>20</sup> that combining HgTe and HgSe into a colloiddally grown heterostructure might be a path to design high performance intraband photoconductor material. The electronic spectrum of such heterostructure is nevertheless quite difficult to appreciate because of the combination of inverted band structure from the bulk material, presence of quantum confinement, strain due to the lattice mismatch, nature of the heterostructure and possible sensitivity to the surface chemistry.<sup>21,22</sup> In order to uncouple these different effects, each contribution needs to be quantified separately. The effect of the size (*ie* the quantum confinement) on the band alignment of HgSe<sup>22</sup> and HgTe<sup>4</sup> has already been reported.<sup>23</sup> Similarly, the change of the band alignment with the surface grafting of molecule has been reported by Robin *et al.*<sup>21</sup>, Martinez *et al.*<sup>22,24</sup> Pressure contributions still needs, on the other hand, to be quantified.

Interestingly, the effect of pressure on HgTe and HgSe has been widely studied for the bulk material,<sup>25,26</sup> motivated by the need for identification of the inverted band structure and the determination of the band gap energy. More recently, HgTe thin films under strain have been revisited as a strategy to generate topological insulators.<sup>27-29</sup> In the bulk and under zero pressure, HgTe crystallizes in a zinc blende structure ( $F\bar{4}3M$ ). The latter transforms into a cinnabar phase<sup>30,31</sup> ( $P3_121$ ) at 1.4 GPa which is stable up to 8 GPa.<sup>32</sup> This phase then turns into the rock salt structure above 8 GPa. Other phases also exist at even higher pressure, but their nature seems controversial.<sup>33</sup> HgSe presents a similar trend, but with different transition pressures.<sup>34</sup> In this paper, we will focus on the low pressure range, typically from 0 to 4 GPa. This range of pressures corresponds to the one expected from lattice-mismatch strain induced on a HgSe core while growing a HgTe shell (1 to 2 GPa).<sup>20</sup>

## METHODS

**Chemicals for nanocrystal synthesis:** Mercury chloride ( $\text{HgCl}_2$ , Strem Chemicals, 99%), Tellurium powder (Te, Sigma-Aldrich, 99.99%), trioctylphosphine (TOP, Cytek, 90%), oleic acid (Sigma, 90%), oleylamine (Acros, 80-90%), dodecanethiol (DDT, Sigma-Aldrich, 98%), chloroform (Carlo Erba), ethanol absolute anhydrous (Carlo Erba, 99.9%), methanol (Carlo Erba, 99.8%), toluene (Carlo Erba, 99.3%), All chemicals are used as received, except oleylamine which is centrifuged before used. **Mercury compounds are highly toxic. Handle them with special care.**

**1 M TOP:Te precursor:** 2.54 g of Te powder is mixed in 20 mL of TOP in a three neck flask. The flask is kept under vacuum at room temperature for 5 min and then the temperature is raised to 100 °C. Furthermore, degassing of flask is conducted for the next 20 min. The atmosphere is switched to Ar and the temperature is raised to 275 °C. The solution is stirred until a clear orange coloration is obtained. The flask is cooled down to room temperature and the color switches to yellow. Finally, this solution is transferred to an Ar filled glove box for storage.

**HgTe CQD synthesis with band edge at 6000  $\text{cm}^{-1}$ :** 513 mg of  $\text{HgCl}_2$  was added to 60 mL of oleylamine in a 100 mL round flask. The solution was placed under vacuum and heated to 110 °C for 1 h. Then, the temperature is decreased to 60°C and solution placed to Ar atmosphere. 1.9 mL of TOP:Te (1 M) with 10 mL of oleylamine are added to the mercury solution. The solution color gradually turns to dark brown and the reaction is stopped at 3 min. A solution made of 1mL of dodecanethiol and 9 mL of toluene is quickly added to quench the reaction. The nanocrystals are then precipitated with ethanol. After centrifugation, the nanocrystals are redispersed in chloroform. The washing step is repeated one more time. The solution is redispersed in chloroform and filtered with a 0.2  $\mu\text{m}$  filter. Additional two washing steps are applied with final redispersion in chloroform.

**HgTe CQD synthesis with band edge at 4000  $\text{cm}^{-1}$ :** 513 mg of  $\text{HgCl}_2$  was added to 60 mL of oleylamine in a 100 mL round flask. The solution was placed under vacuum and heated to 110 °C for 1 h. Then, the temperature is decreased to 80 °C and solution placed to Ar atmosphere. 1.9 mL of TOP:Te (1 M) with 10 mL of oleylamine are added to the mercury solution. The solution color gradually turns to dark brown and the reaction is stopped at 3 min. A solution made of 1 mL of dodecanethiol and 9mL of toluene is quickly added to quench the reaction. The nanocrystals are then precipitated with ethanol. After centrifugation, the nanocrystals are redispersed in chloroform. The washing step is repeated one more time. The solution is filtered with a 0.2  $\mu\text{m}$  filter and redispersed in 6mL of chloroform.

**1 M TOP:Se precursor:** 1.57 g of Se is mixed with 20 mL of TOP in a flask. Dissolution of Se powder is helped by sonication for 1 hour. The resulting solution is colorless.

**HgSe CQD synthesis with band edge at 3000  $\text{cm}^{-1}$ :** 0.5 g of mercury acetate are dissolved in 10 mL of oleic acid and 25 mL of oleylamine. The solution is degassed under vacuum at 100 °C during 60 min. The atmosphere is switched to argon. At 110 °C, 1.6 mL of TOP:Se (1 M) is injected to the mercury solution. The solution rapidly turns from yellow to dark, indicating the formation of HgSe material. After 1 min, the reaction is quenched by adding 1 mL of dodecanethiol and cooled to room temperature with air flux. The nanocrystals are then precipitated with ethanol. After centrifugation, the nanocrystals are redispersed in chloroform. The washing step is repeated one more time. The solution is filtered with a 0.2  $\mu\text{m}$  filter and redispersed in 6 mL of chloroform. Two size selection precipitations are carried out by adding ethanol and keeping the precipitate each time.

**HgSe CQD synthesis with band edge at 2500  $\text{cm}^{-1}$ :** 0.5 g of mercury acetate are dissolved in 10 mL of oleic acid and 25 mL of oleylamine. The solution is degassed under vacuum at 100 °C during 60 min. The atmosphere is switched to argon. At 110 °C, 1 mL of TOP:Se (1 M) is injected to the mercury solution. The solution rapidly turns from yellow to dark, indicating the formation of HgSe material. After 1 min, the reaction is quenched by adding 1 mL of dodecanethiol and cooled to room temperature with water bath. The nanocrystals are then precipitated with ethanol. After centrifugation, the nanocrystals are redispersed in chloroform. The washing step is repeated one more time. The solution is filtered with a 0.2  $\mu\text{m}$  filter and redispersed in 6 mL of chloroform.

**HgSe CQD synthesis with band edge at 1000 cm<sup>-1</sup>:** 0.5 g of mercury acetate are dissolved in 10 mL of oleic acid and 25 mL of oleylamine. The solution is degassed under vacuum at 100 °C during 60 min. The atmosphere is switched to argon. At 110 °C, 0.65 g of SeS<sub>2</sub> dissolved in 5 mL of OLA is injected to the mercury solution. The solution rapidly turns from yellow to dark, indicating the formation of HgSe material. After 1 min, the reaction is quenched by adding 1 mL of dodecanethiol and cooled to room temperature with water bath. The nanocrystals are then precipitated with ethanol. After centrifugation, the nanocrystals are redispersed in chloroform. The washing step is repeated one more time.

**Electron microscopy:** For TEM pictures, a drop of CQD solution is drop-casted on a copper grid covered with an amorphous carbon film. JEOL 2010F is used at 200 kV for acquisition of pictures. For device characterization, FEI Magellan scanning electron microscope is used.

**Diamond Anvil Cell loading for X-ray diffraction:** Experiments were carried out using a membrane diamond anvil cell equipped with Boehler-type anvils with 500 micrometer culets. A stainless-steel gasket of 200 micrometer thickness was pre-indented to 70 µm, provided with a 200 µm hole, and loaded with the sample, a 4:1 methanol-ethanol pressure transmitting medium and a 10 µm diameter ruby sphere which served as pressure marker. The "Mao hydrostatic" pressure scale was used to determine pressures.

**X-ray diffraction under pressure:** X-Ray powder diffraction measurements were carried out at the XRD platform of the IMPMC on a Rigaku MM007HF diffractometer equipped with a Mo rotating anode ( $\lambda_{K\alpha 1} = 0.709319 \text{ \AA}$ ,  $\lambda_{K\alpha 2} = 0.713609 \text{ \AA}$ ), Varimax focusing optics and a RAXIS4++ image plate detector. X-ray data were collected at 20°C. A LaB<sub>6</sub> standard sample was measured in the same experimental conditions to calibrate the Fit2D program, the image processing software used to integrate the intensities around the Debye-Scherrer rings and to get the 1D patterns.

**Diamond Anvil Cell loading for IR spectroscopy:** Membrane diamond anvil cells (DACs), equipped with a diamond and 400-500 µm culets, are used. Stainless steel gaskets with a thickness of 200 µm are indented down to 50 µm. A 150 µm hole is then drilled by electro-erosion. The gasket is placed on the top of one of the DAC diamond, then filled with NaCl. After a ruby crystal is introduced, the DAC is closed under gentle pressure until the salt forms a clear window. A drop of a diluted suspension of CQDs in chloroform, chlorobenzene or toluene is then added and dried on top of the NaCl window to form a dry, uniform film of CQDs. The DAC is then closed and introduced in the Cassegrain microscope.

**Infrared spectra under pressure:** the DAC is pressurized by the means of a metallic membrane inflated with He gas. The *in situ* pressure is monitored by the means of a photoluminescence setup. A 532 nm laser is shone through one of the Cassegrain objectives and focused on the ruby crystal embedded in the cell. Ruby photoluminescence light is collected and sent to an OceanOptics spectrometer, showing a characteristic doublet around 694 nm at ambient pressure. This photoluminescence is fitted and the pressure is computed using the main peak position. Once the pressure is stabilized, an infrared absorbance spectrum is acquired using a Thermo Fisher Nicolet iS50 FTIR with the synchrotron light as a source and an MCT detector in transmission configuration. This operation is repeated with steps of 0.5 GPa from 0 GPa to 4 GPa, then steps of 1 GPa up to 10 GPa. When the maximum pressure is reached, the membrane is deflated and several spectra are acquired to check the reversibility of the pressure effect.

## DISCUSSION

We have synthesized series of HgTe and HgSe CQDs with three different sizes for each material, using previously reported methods<sup>12,35</sup>. The supporting information (SI) provides more details about synthesis. HgTe CQDs of 6 nm and 8 nm present a band edge at 6000 and 4000 cm<sup>-1</sup> respectively, see Figure 1a and S1 for infrared spectra after synthesis (*ie* under zero pressure). The optical spectrum is typical for quasi-intrinsic semiconductor with no absorption at long wavelengths and the presence of a tunable feature at the bandgap of the material. This feature is followed by a

broadband absorption at shorter wavelengths. The particles adopt a tetrapodic shape, as revealed by transmission electron microscopy (TEM), see Figure 1b.

In the case of HgSe, three samples have been prepared. The infrared spectra reveal two components. In the near infrared part of the spectrum, interband transitions appear as broadband absorption features (same as HgTe). In the mid infrared range, the spectra reveal an additional peak, see Figure 1c. This peak corresponds to an intraband transition, signature of the degenerative doping<sup>17,18,22</sup> of the material resulting from a self-doping mechanism.<sup>21</sup> Both absorption features red-shift when the size of the material is increased, see Figure 1d. The three sizes of synthesized CQDs have respectively intraband absorption at 3000, 2500 and 1000  $\text{cm}^{-1}$ . The particles come with a more spherical shape than HgTe, as shown on the TEM image, see Figure 1d and S2.

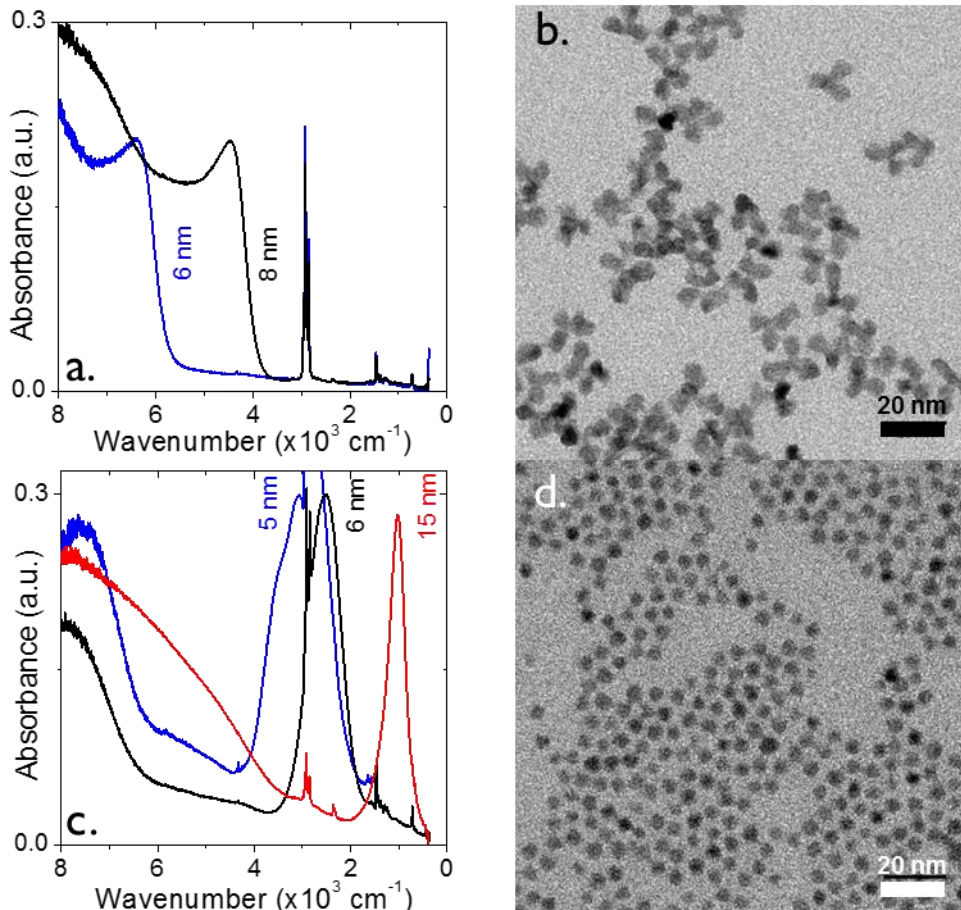


Figure 1 : a. Infrared spectra of two different sizes (6 and 8 nm) of HgTe CQDs, under zero pressure. b. TEM image of HgTe CQDs with a band edge energy at  $4000 \text{ cm}^{-1}$ . c. Infrared spectra of three different sizes (5, 6 and 15 nm) of HgSe CQDs, under zero pressure. d. TEM image of HgSe CQDs with an average size of 5nm presenting an intraband transition at  $2500 \text{ cm}^{-1}$ .

Since the targeted range of pressure (0-4 GPa) overlaps with known crystallographic phase transitions of the bulk material, we have first probed the crystallographic structure of our material using X-ray diffraction, see Figure 2. The X-ray pattern obtained for HgTe  $4000 \text{ cm}^{-1}$  (ie 8 nm in size), see Figure 2a, reveals that the zinc blende phase remains present at least up to 3 GPa. At 5 GPa, we observe a clear phase change towards the cinnabar phase, see Figure S3. We estimate the structural parameter of the hexagonal phase of HgTe to be  $a=b=0.447 \text{ nm}$  and  $c=0.943 \text{ nm}$  under 5.5 GPa of pressure.

Compared to bulk for which the threshold pressure is  $1.4 \text{ GPa}$ <sup>29-31</sup>, the threshold pressure is strongly increased.<sup>36</sup> This effect actually results from hysteresis in the phase transition, which was previously attributed to nucleation barrier.<sup>37</sup>

Similarly, a lack of phase transition has been observed in HgTe/HgCdTe superlattice,<sup>34</sup> however the authors did not confirm that the zero pressure crystal structure was indeed preserved. Following the shift of the reflections with pressure in the zinc blende phase, we extract a pressure coefficient of the lattice parameter of  $da/dP = -6.4 \times 10^{-3}$  nm/GPa around the smallest probed pressure of 1 GPa and average lattice parameter  $a \approx 0.645$  nm, see Figure 2b and c. This corresponds to a bulk modulus at zero pressure  $B_{\text{HgTe}} = -dP/(3da/a) \approx 33$  GPa, very close to the value of 34 GPa expected for bulk HgTe.<sup>38</sup> Assuming a Poisson coefficient of 0.288,<sup>38</sup> we can estimate the experimental Young modulus to be 42 GPa, again very close to the value of 40 GPa commonly admitted for bulk HgTe.<sup>39</sup> We observe that the bulk modulus significantly decreases with pressure, with an amplitude of 21 GPa around 3 GPa pressure, a signature of the beginning of the transition towards the cinnabar phase.

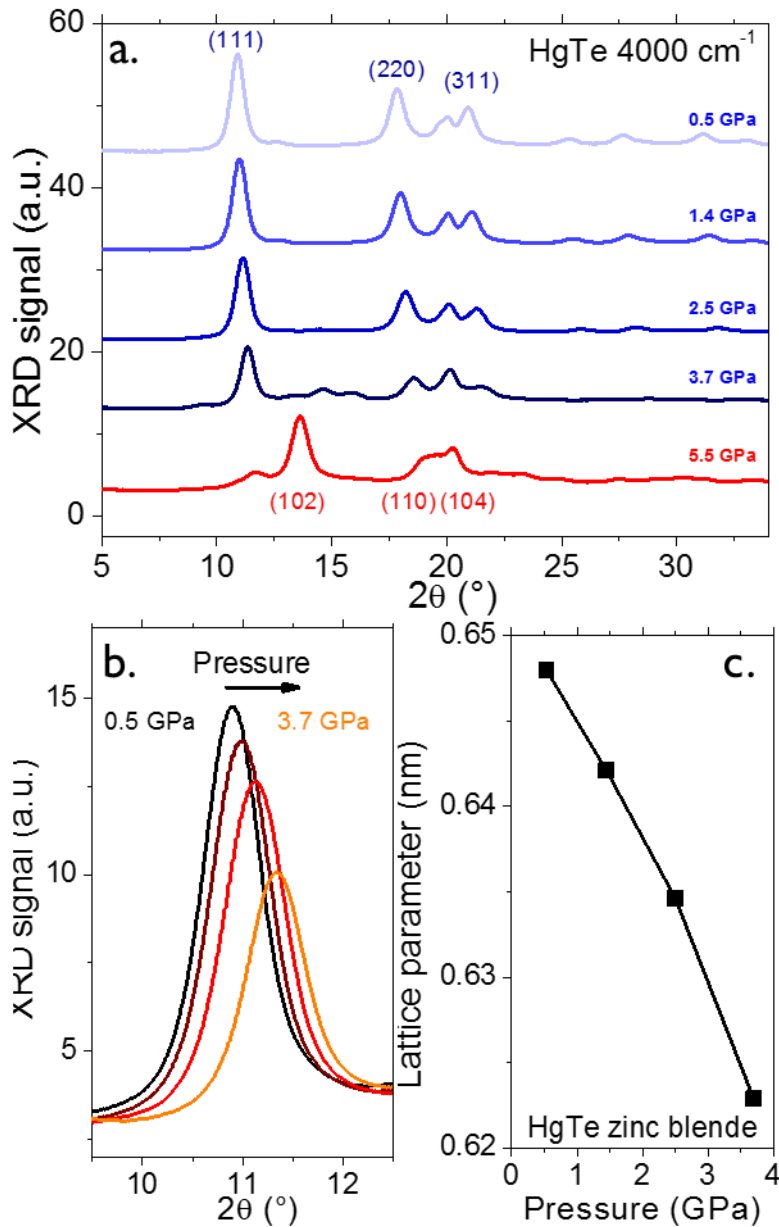


Figure 2 : a. Diffraction pattern of HgTe CQDs (with a band edge at zero pressure at  $4000 \text{ cm}^{-1}$ ) under different pressures. b. Zoom on the (111) Bragg reflection of HgTe CQDs (with a band edge at zero pressure at  $4000 \text{ cm}^{-1}$ ) under different pressures while the material remains in the zinc blende phase (ie  $P < 4$  GPa). c Lattice parameter of the zinc blende phase as a function of pressure.

Infrared spectroscopy under pressure was carried out on the SMIS beamline of Synchrotron Soleil. The CQDs are introduced in a diamond anvil cell (DAC) and the transmission infrared spectrum is acquired using infrared synchrotron

light as a source, see Figure 3 for a scheme of the setup. The CQD-containing DAC is placed between the two custom-made Cassegrain objectives, which focus the IR light on the 150  $\mu\text{m}$  sample chamber drilled in the DAC gasket. The transmitted light is collected by a MCT (HgCdTe) detector and the signal is processed by a FTIR spectrometer (Thermo Fisher iS 50). The pressure in the cell is increased by inflating a metal membrane, and the pressure is obtained *in situ* through the measurement of the fluorescence signal of a ruby crystal loaded in the DAC near the sample, see supporting informations. Raw infrared spectra feature high frequency oscillations resulting from interferences within the diamond cell. The latter are removed using FFT filtering, see figure S4.

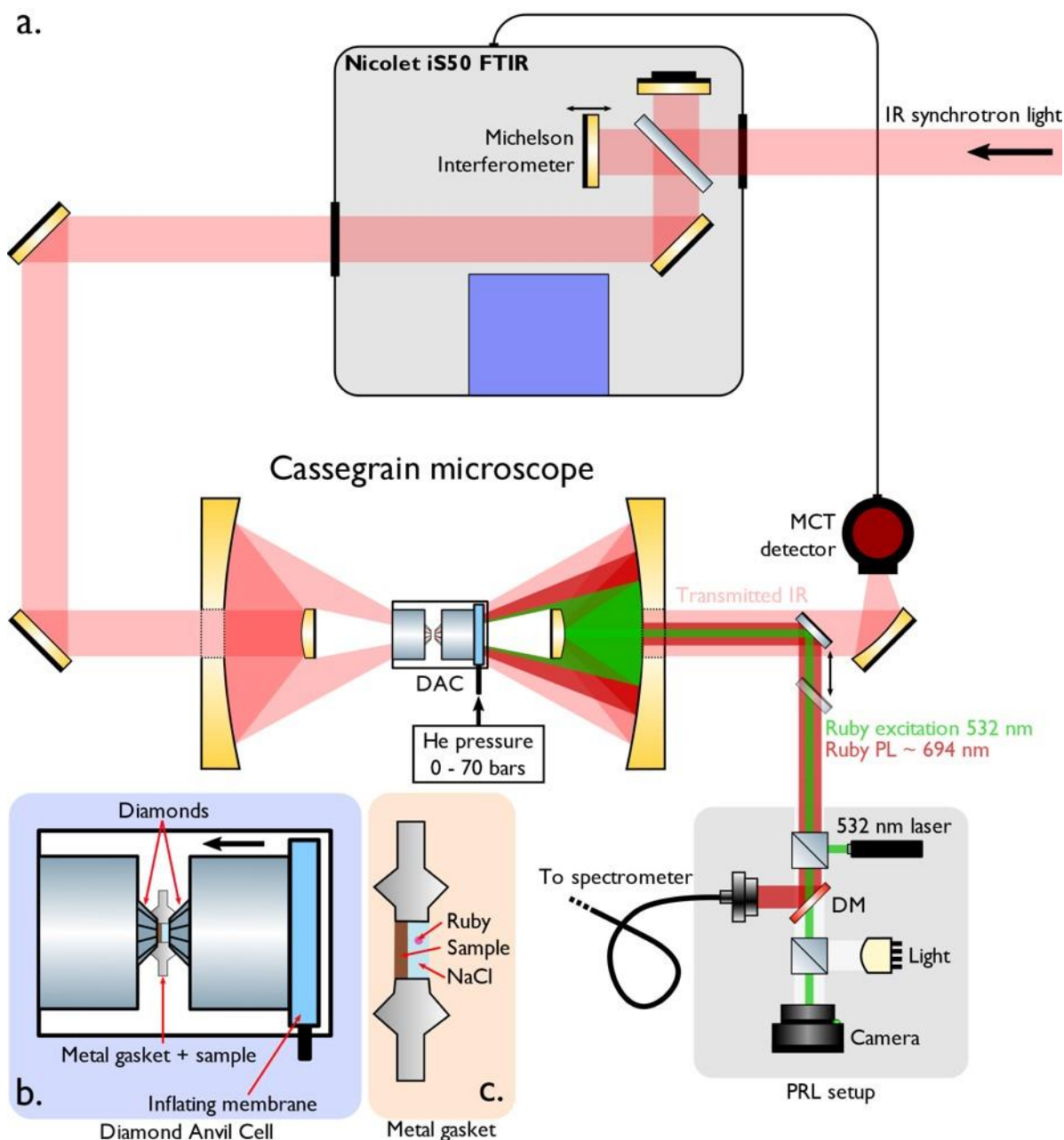


Figure 3 : a. Scheme of the optical setup used to obtain infrared spectra of the HgX nanocrystals under pressure. Synchrotron light is used as broad band infrared source. The pressure within the diamond cell is measured through the shift of the ruby luminescence. DAC: Diamond Anvil Cell. PRL: Pressure by Ruby Luminescence spectrometer. DM: Dichroic Mirror. b. Scheme of diamond anvil cell. c. Scheme of the inner part of the diamond anvil cell containing the actual nanocrystal sample.



In the case of HgTe, we have observed a strong blue-shift of the interband signal as the pressure is increased, see Figure 4a. Above 3 GPa, the spectrum becomes featureless and the background keeps increasing, see Figure 4a and S4. It is worth noticing that infrared and X-ray measurements present consistent changes: the loss of excitonic feature on the infrared spectrum occurs in the same pressure range as the structural phase changes (3-4 GPa). Note that up to 10 GPa, the maximum pressure in our experiment, the change of the signal is reversible, even though we observe hysteresis.<sup>37,40,41</sup>

The shift of the band edge with pressure for the two sizes of CQDs is summarized in Figure 4b. In the low range of pressure (*ie* below 2 GPa), the shift is linear with pressure and allows us to extract a value for  $\frac{dE_{inter}}{dP} \approx 60 \text{ meV/GPa}$ , independent of the CQD size. For sake of comparison CdSe nanocrystals<sup>42</sup> presents a twice smaller (38 meV/GPa) shift. This value can be compared with the pressure shift induced by temperature. HgTe presents an inverted temperature dependence (*ie* the interband transition redshifts under cooling) with a  $\frac{dE_{inter}}{dT} \approx 300 \mu\text{eV/K}$ .<sup>15</sup> In other words, applying 1 GPa is equivalent to increasing the temperature of the sample by 200 K. In this sense, pressure allows to explore changes in the electronic structure which are way out of the temperature stability range of the colloidal material.

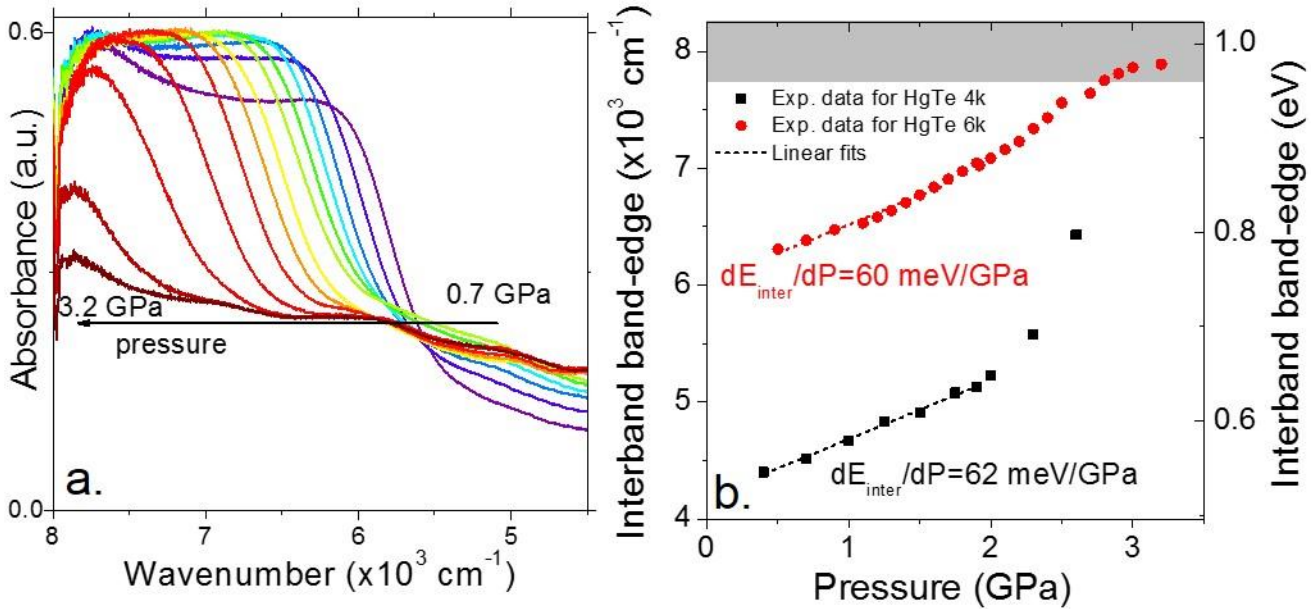


Figure 4 : a. Infrared spectrum of HgTe CQDs, with a zero-pressure band edge around  $6000 \text{ cm}^{-1}$ , under increasing pressure. b. Interband band edge energy as a function of the applied pressure for two populations of HgTe CQDs: with a band-edge around  $4000 \text{ cm}^{-1}$  (HgTe 4k, in black) and with a band-edge around  $6000 \text{ cm}^{-1}$  (HgTe 6k, in red). In the 1-2 GPa range, where a linear fit is possible (dashed lines), the value of  $dE/dP$  is indicated.

To further understand the origin of this shift, it is important to remind that in HgTe CQDs, the interband transition occurs between the two  $\Gamma_8$  symmetry bands. As bulk HgTe is a vanishing band gap semiconductor, the energy difference between these two bands at  $\Gamma$  point of the Brillouin zone is 0. In a simplistic, infinite well quantum box model, the band edge energy is given by  $E_{inter}(P) = E_{bulk}(P) + \frac{3\hbar^2\pi^2}{2m_h^*(P)(2R_{QD}(P))^2} + \frac{3\hbar^2\pi^2}{2m_e^*(P)(2R_{QD}(P))^2}$ . Even though basic, the  $R^{-2}$  scaling for the size dependence of the band edge energy of HgTe nanocrystals was previously observed experimentally<sup>15</sup>. In this expression  $\hbar$  is the reduced Planck's constant,  $E_{bulk}(P)$  is the bulk optical band gap (with  $E_{bulk}(P = 0) = 0$ ),  $m_h^*$  and  $m_e^*$  are respectively the hole and electronic effective masses and  $R_{QD}$  the half-size of the box referred to as the nanocrystal "radius" in what follows. We also write the simple parametrized expression:  $E_{inter} =$

$E_{\text{bulk}} + \frac{\hbar^2 k^2}{2m^*}$  where  $k = \frac{\sqrt{3}\pi}{2R_{\text{QD}}}$  is the norm of the discretized wave vector and  $m^*$  the equivalent mass that gives the energy  $E_{\text{inter}}$ .

Then, the observed shift may result from three origins: (i) a change in the bulk band gap (which is zero under zero pressure), (ii) a change in the effective masses and/or (iii) a change in the size of the CQDs. Due to the application of pressure, the nanocrystal size shrinks. Using the  $B_{\text{HgTe}} = 33$  GPa bulk modulus determined from X-ray diffraction, we can estimate that applying  $P=1$  GPa of pressure leads to a  $P/3/B_{\text{HgTe}} \approx 1.0\%$  reduction in the nanocrystal size. This CQD size reduction is expected to lead to more confinement and thus a blue-shift would be expected. In the hypothesis of a parabolic band in the infinite well model, the relative shift resulting from the change of nanocrystal size under pressure is  $\frac{\Delta E_{\text{inter}}(P)}{E_{\text{inter}}(P=0)} = 2 \frac{\Delta R_{\text{QD}}}{R_{\text{QD}}(P=0)} \approx \frac{2P}{E_{\text{HgTe}}} \approx 2\%$ .

This is significantly smaller than the experimentally observed relative energy shift, which is around 10% in Figure 4b. We can anticipate the change in the band structure of compressively strained bulk HgTe to represent a significant contribution to the observed energy shifts. Indeed, the pressure dependence of the interband gap has been reported to be  $\approx 70$  meV/GPa for bulk HgTe<sup>43</sup> and HgTe based superlattice,<sup>44</sup> which is quite close to the value measured on nanocrystals.

To reveal the pressure effect on bulk HgTe, we use a Pidgeon-Brown 8-band  $\mathbf{k}\cdot\mathbf{p}$  formalism as described in the SI. In short, the  $\mathbf{k}\cdot\mathbf{p}$  multiband structure is first fitted at zero strain to the one predicted by A. Svane *et al.*<sup>45</sup> based on a hybrid quasi-particle self-consistent Green's function screened Coulomb interaction scheme "h-QSGW", see figure S6a. The effect of strain is then accounted for through the application of a deformation potential of  $\alpha_{\text{HgTe}} = -2.4$  eV between  $\Gamma_8$  and  $\Gamma_6$  bands, chosen to fit the pressure dependent shifts. The deformation potential defines the band-edge energy change  $d(E_{\Gamma_6} - E_{\Gamma_8})$  with the change  $da$  of the lattice parameter  $a$  following the relation  $d(E_{\Gamma_6} - E_{\Gamma_8}) = 3\alpha_{\text{HgTe}} da/a$ . Note that  $\alpha_{\text{HgTe}}$  and the compressive strain  $\epsilon = da/a$  are both negative, leading to an increase of the energy difference  $E_{\Gamma_6} - E_{\Gamma_8}$  with increasing pressure. The band structure of HgTe at zero strain is reported in Figure 5a around the zone center for various compressive strains  $\epsilon$ . It is compared to the Dresselhaus-Kip-Kittel formula, given in the SI, for the  $\Gamma_8$  bands plotted as a thin green line. This formula is parabolic along each fixed  $\mathbf{k}$  direction. The comparison shows that the energy dispersion of the conduction band becomes highly non-parabolic a few percent away from the Brillouin zone center.

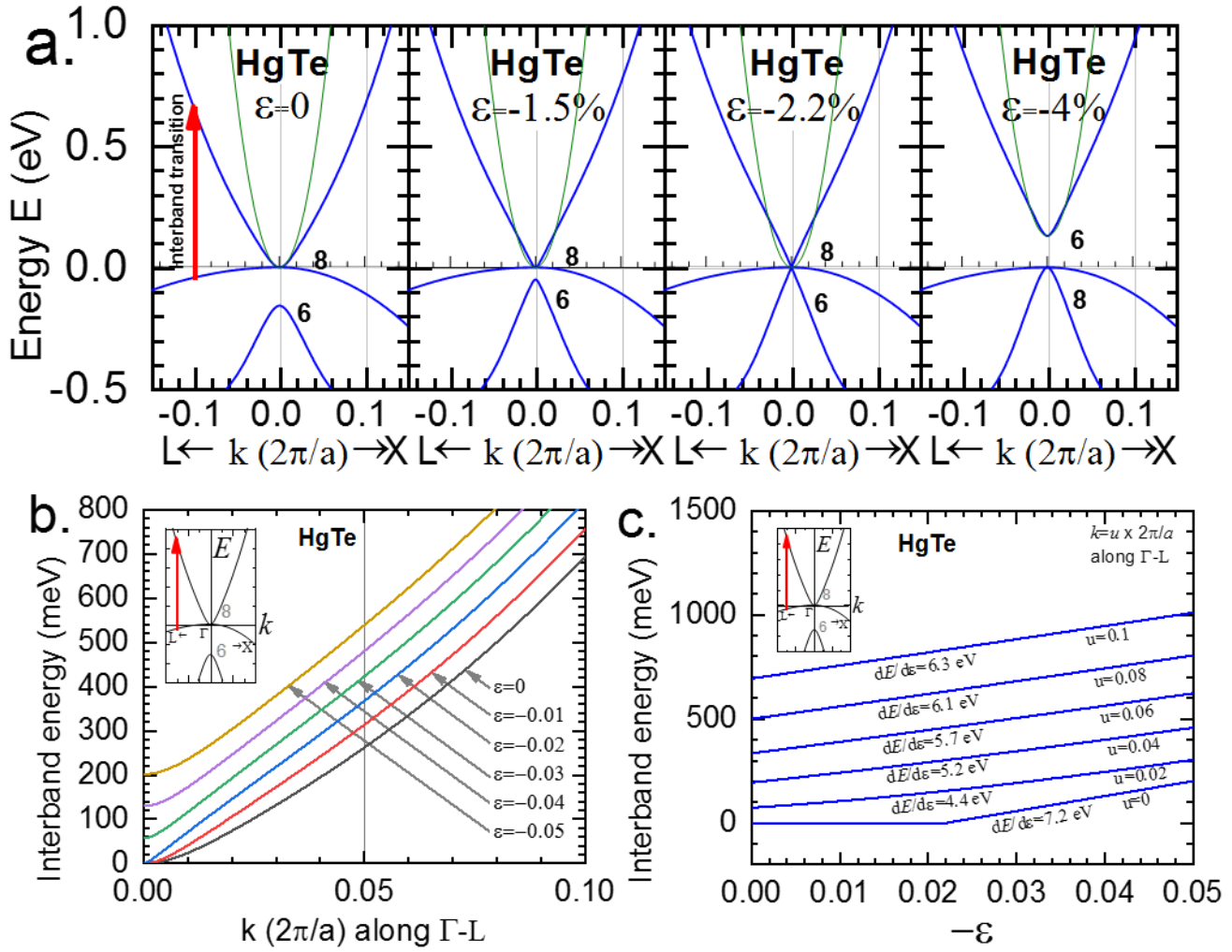


Figure 5 a. Energy dispersion of HgTe calculated for strain  $\epsilon$  varying from 0 (unstrained) to -4% as a function of Brillouin zone wave vector  $k$ . The gap remains closed (zero) up to  $\epsilon = -2.2\%$ . The thin green line is identical for all deformations and corresponds to the Dresselhaus-Kip-Kittel formula, parabolic along each of the  $\Gamma - X$  and  $\Gamma - L$  directions. b. Energy of the interband transition as a function of wavevector (i.e. for various particle sizes) for different deformation values. c. Interband transition energy  $E$  in strained bulk HgTe at several  $k_{111}$  points along [111] direction of the Brillouin zone, as schematically depicted in the inset. The slope  $dE/d\epsilon$  is extracted at strain  $\epsilon = -2.5\%$ .

When strain is applied compressively, the calculated interband energies strongly blue-shift (see Figure 5b) following two successive regimes. First at small strain,  $|\epsilon| \leq 0.022$ , the band gap remains null since the  $\Gamma_6$  states stay below the  $\Gamma_8$  ones. But the effective mass of the conduction band strongly decreases (i.e. the conduction band curvature increases), leading to a blue shift of  $E_{inter}$ . Second, at larger strain  $|\epsilon| > 0.022$ , the gap opens when the  $\Gamma_6$  state energy moves above the  $\Gamma_8$  one. As the bandgap is opening, the effective mass decreases and tends to recover its original value (see Figure S6b).

Interestingly, the equivalent mass, which is the effective mass  $m^*(\mathbf{k})$  that gives the energy  $E(\mathbf{k})$  of the conduction band (calculated through the  $\mathbf{k}\cdot\mathbf{p}$  model) at the  $\mathbf{k}$  point in the parabolic formula  $E(k) = E(k=0) + \frac{\hbar^2 k^2}{2m^*(k)}$ , does not vary by a large amount through the introduction of deformation, see Figure S6b. This supports *a posteriori* the use of the parabolic model despite the bands displaying strong non-parabolicity.

Since the fundamental electron and hole states in the nanocrystals are expected to be constructed from Bloch functions with a wavevector around  $\mathbf{k}_{\pm 1 \pm 1 \pm 1} = \frac{\pi}{2R_{QD}}(\pm 1, \pm 1, \pm 1)$  at energies  $E_e$  and  $E_h$ , we look at the energy change  $E_{inter}(\mathbf{k}, \epsilon) = E_e(\mathbf{k}, \epsilon) - E_h(\mathbf{k}, \epsilon)$  at these fixed symmetrically-equivalent wavevector locations  $\mathbf{k}$  in the Brillouin zone, as depicted in the inset of Figure 5b. The two regimes of pressure effect described previously appear clearly in the dependence of  $E_{inter}$  at  $\mathbf{k} = \mathbf{0}$  (*i.e.*  $u = k/(2\pi/a) = 0$ ) as a function of  $\epsilon$  in Figure 5c. However, at a wavevector  $\mathbf{k}_{111}$  away from the zone center, these two regimes are undistinguishable because the gap opening at large strain mimics the effective mass drop at small strain. At energies of few hundreds of meV, the dependence of the interband energy appears nearly linear, as observed experimentally, with a slope between 5.7 eV and 6.3 eV, see Figure 5c. This slope corresponds closely to the slope of the strain induced  $\Gamma_6 - \Gamma_8$  energy variation *i.e.* 3 times the -2.4 eV deformation potential, confirming the interplay between the effective mass drop and gap opening. Considering the measured bulk modulus of 33 GPa, this leads to an observed  $\approx 60$  meV/GPa blue shift weakly dependent on the  $\mathbf{k}$  vector, *i.e.* the radius. This simple model reproduces the sign and the pressure dependence of the interband gap shifts, as well as the fact that this shift does not depend strongly on the nanocrystal size. The used deformation potential of -2.4 eV is much smaller than the -3.69 eV as measured by Latussek et al<sup>44</sup> for a HgTe/HgCdTe superlattice. This difference is likely the result of the presence of long organic ligands which affect the deformation potential value in the case of nanocrystals and also from the presence of Cd in the work of Latussek.

The pressure dependence of the intraband transition has then been investigated into HgSe nanocrystals presenting intraband absorption. As presented in the beginning of discussion (Figure 1d), the IR spectrum of this material shows interband contributions at high energy and its pressure dependence is similar to the one observed for HgTe, with a blue-shift of the transition while increasing pressure. On the other hand, the intraband contribution of the spectrum is red-shifting with increasing pressure, see Figure 6a. In addition, the shift presents a size dependence: the redder the intraband peak under zero pressure, the smaller the shift, see Figure 6a.

The understanding of the redshift associated with the intraband transition is the combined effect of strain-induced depopulation, change of oscillator strength and possible increase of the intraband mass. We thus choose to provide a phenomenological description of this process based on the parametrized intraband energy  $E_{intra}(P) = E_{intra}(P=0) + \frac{\hbar^2 k^2}{2m_{intra}^*(P)}$  where  $m_{intra}^*(P)$  is the intraband equivalent mass giving the transition energy  $E_{intra}(P)$ . First, note that in the real space, as for the interband contribution, the application of pressure leads to a QCD size reduction. As a result, the  $E_{intra}(P) \propto \frac{1}{R_{QD}^2(P)}$  scaling is expected to lead to a blue-shift of the transition, whereas a red-shift is observed in Figure 6b. This means that the pressure dependence of the size effect is completely balanced by that of the intraband equivalent mass. The size effect is slightly overcome by that of the mass, explaining the low magnitude of the intraband redshift ( $9 \pm 2$  meV/GPa) compared to the interband blueshift magnitude (60 meV/GPa).

In the low range of pressure where the intraband energy peak shifts linearly, one can write  $E_{intra}(P) \sim E_{intra}(P=0) + \frac{dE_{intra}}{dP} \cdot P$  and  $R(P) \sim R(P=0)(1 - P/3/B_{HgSe})$ , with  $B_{HgSe}$  the bulk modulus of HgSe. Thus, one can extract the pressure dependence of the equivalent mass for the conduction band  $\frac{m_{intra}^*(P)}{m_{intra}^*(P=0)} = \frac{R^2(P=0) \cdot E_{intra}(P=0)}{R^2(P) \cdot E_{intra}(P)} \sim \frac{1}{\left[1 + \frac{dE_{intra}}{dP} \cdot \frac{P}{E_{intra}(P=0)}\right] \left[1 - \frac{P}{3B_{HgSe}}\right]^2}$ . Using this equation, the change of the intraband equivalent mass under pressure for  $2500 \text{ cm}^{-1}$  HgSe QCDs has been deduced and is given in Figure 6c. As  $dE_{intra}/dP$  is negative, this leads to an intraband mass which is higher under pressure than at 0 GPa. Typically, the mass increases by 5% per GPa under pressure application. In other words, the application of pressure tends to flatten the conduction band (*i.e.* reduce its dispersion).

The intraband redshift also comes with a drastic reduction of the peak intensity, see Figure 6a. The latter results from bulk band gap opening, as previously seen in the case of HgTe. As the band gap opens, the 1Se level moves towards vacuum and gets closer to the Fermi level. This tends to reduce the degenerate doping and leads to the observed reduction in intensity of the intraband transition peak.

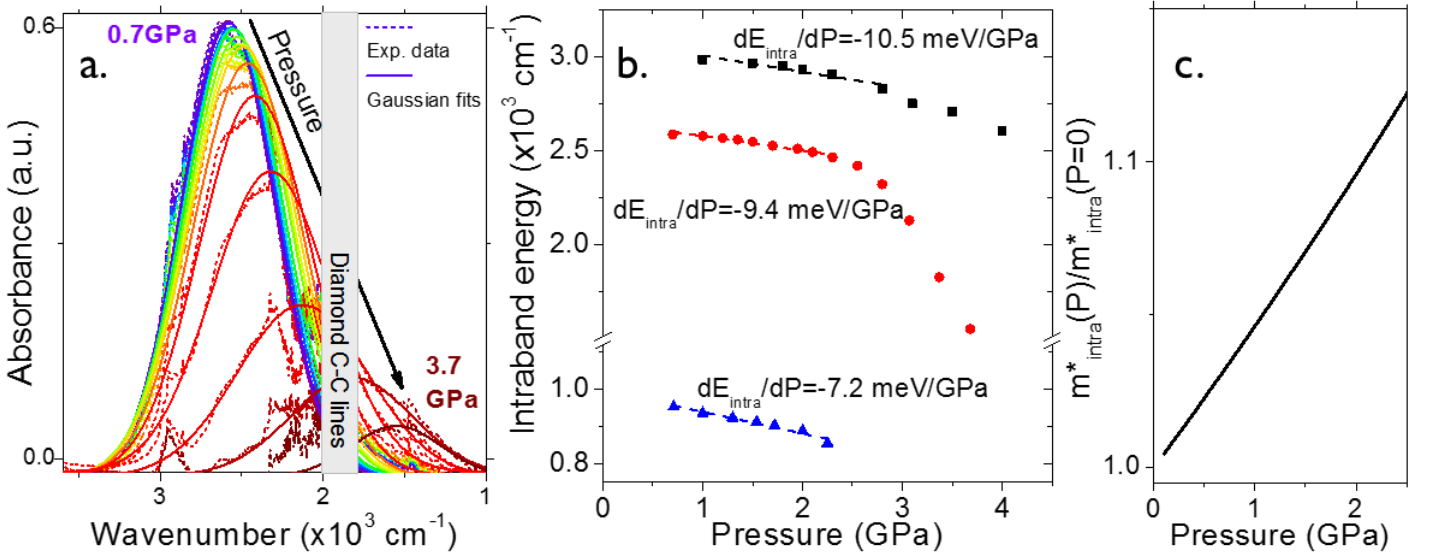


Figure 6 : a. Infrared spectrum of HgSe CQDs, with a zero pressure intraband feature at  $2500 \text{ cm}^{-1}$ , under various pressures. Raw data is provided in dashed lines, and solid lines are the Gaussian fits of the intraband peak. b. Intraband band edge energy as a function of the applied pressure for three populations of HgSe CQDs ( $3000 \text{ cm}^{-1}$  in black,  $2500 \text{ cm}^{-1}$  in red and  $1000 \text{ cm}^{-1}$  in blue). In the 1-2 GPa range, where a linear fit is possible the value of  $dE/dP$  is indicated. c. Change of the conduction band effective mass as a function of the applied pressure for the HgSe CQDs with an intraband feature at  $2500 \text{ cm}^{-1}$ .

The results we obtained can be used to determine the pressure influence on complex structure such as core-shell QDs. Goubet et al.<sup>20</sup> recently reported the growth of HgSe/HgTe core shell heterostructure that combine the best of the two materials (*ie* the intraband transition of HgSe, with the fast response, high activation energy and low dark current of HgTe). Because HgTe has a larger lattice parameter than HgSe, HgTe shell is under compression while HgSe core is under tensile strain. It has been observed that as the HgTe shell grows, the intraband transition remains almost unaffected, while the interband is strongly red-shifted. The interfacial pressure  $P_0$  was estimated<sup>46</sup> to be

$$P_0 = \frac{2E\varepsilon \left( \frac{R_{\text{shell}}^3}{R_{\text{core}}^3} - 1 \right)}{3(1-\nu) \frac{R_{\text{shell}}^3}{R_{\text{core}}^3}} \approx 1.4 \text{ GPa}$$

with  $E$  (40 GPa) and  $\nu$  (0.46) respectively the Young modulus and the Poisson

coefficient (assumed to be the same for the core and the shell<sup>20</sup>),  $R_{\text{core}}$  and  $R_{\text{shell}}$  are the radii of the core and the shell, taken as 2.6 and 3.2 nm respectively, and  $\varepsilon$  is the lattice mismatch between HgTe and HgSe, equal to 0.06. In such heterostructure, the electron is confined in HgSe and the very small red-shift on intraband contribution resulting from the HgTe growth can indeed be due to pressure-induced effects. On the other hand, in the case of the interband transition, a 1.4 GPa interfacial pressure should lead to a redshift of  $\frac{dE_{\text{inter}}}{dP} \cdot P \approx 84 \text{ meV} \approx 680 \text{ cm}^{-1}$ . This is much smaller than the experimentally observed shift which is above  $2000 \text{ cm}^{-1}$ . As a result, we can confidently conclude that the shift of the interband transition is mostly the effect of charge delocalization and more specifically the hole moving toward the HgTe shell.<sup>20</sup>

Another important finding is the fact that we can estimate which shell material can be grown without leading to a cinnabar phase change. We showed that HgTe zinc blende phase can be preserved if pressure remains below 3 GPa.

As interfacial pressure is around 1.4 GPa in the case of the HgTe/HgSe heterostructure, the phase of HgTe core is still the zinc blende phase.

To increase HgTe resistance to high temperatures, one can think of growing a CdS shell on a HgTe core. As CdS and HgTe do not present the same elastic properties, the formula to calculate the interfacial pressure between core and shell is the following: <sup>46</sup>

$$P_0 = \frac{2 \cdot E_{core} \cdot E_{shell} \cdot \epsilon \cdot \left( \frac{R_{shell}^3}{R_{core}^3} - 1 \right)}{\left( 2E_{shell}(1 - 2\nu_{core}) + E_{core}(1 + \nu_{shell}) \right) \frac{R_{shell}^3}{R_{core}^3} - 2(E_{shell}(1 - 2\nu_{core}) - E_{core}(1 - 2\nu_{shell}))} = 2.6 \text{ GPa}$$

Where  $E_{core}$  is HgTe Young Modulus equal to 34 GPa,  $E_{shell}$  is CdS Young modulus equal to 70 GPa,  $\epsilon$  is the lattice mismatch (0.10),  $R_{shell}$  and  $R_{core}$  are radius of shell and core respectively and taken equal to 3.2 and 2.6 nm,  $\nu_{core}$  is HgTe Poisson coefficient equal to 0.288 and  $\nu_{shell}$  is CdS Poisson coefficient<sup>47</sup> equal to 0.34. The obtained value of 2.6 GPa value is quite close to the measured threshold value of 3-4 GPa for phase change to cinnabar. To avoid any phase change and the associated dramatic renormalization of the band gap, thinner shell with  $R < 3$  nm could be considered.

## CONCLUSION

We have investigated the effect of pressure on the interband and intraband transition in mercury chalcogenides nanocrystals. The interband transition follows the same blue-shift as the bulk material. However, we have observed that the onset pressure for the transition from zinc blende to the cinnabar phase occurs at much higher pressure than for the bulk. Once the phase change occurs, no more excitonic feature is observed. The intraband transition shows a red shift under pressure. The magnitude of the shift is nevertheless weaker than the one observed for the interband transition. This results phenomenologically from a competition between material contraction leading to a blue-shift and the increase of the intraband equivalent mass leading to a red-shift. Finally, we point that the growth of shell material with a too large lattice mismatch may lead beyond the formation of cracks to a phase change in the core.

## Supporting informations

Additional informations about the material, material characterization and k-p modelling are provided in the supporting informations

## ACKNOWLEDGMENTS

EL thanks the support ERC starting grant blackQD (grant n°756225). We acknowledge the use of clean-room facilities from the "Centrale de Proximité Paris-Centre". This work has been supported by the Region Ile-de-France in the framework of DIM Nano-K (grant dopQD). This work was supported by French state funds managed by the ANR within the Investissements d'Avenir programme under reference ANR-11-IDEX-0004-02 and ANR-10-LABX-0035 for Labex NanoSaclay, and more specifically within the framework of the Cluster of Excellence MATISSE and also by the grant IPER-nano2. NG and JR thank Nexdot for post doc funding.

## REFERENCES

- (1) Kovalenko, M. V.; Kaufmann, E.; Pachinger, D.; Roither, J.; Huber, M.; Stangl, J.; Hesser, G.; Schäffler, F.; Heiss, W. Colloidal HgTe Nanocrystals with Widely Tunable Narrow Band Gap Energies: From Telecommunications to Molecular Vibrations. *J. Am. Chem. Soc.* **2006**, *128* (11), 3516–3517.
- (2) Chen, M.; Lu, H.; Abdelazim, N. M.; Zhu, Y.; Wang, Z.; Ren, W.; Kershaw, S. V.; Rogach, A. L.; Zhao, N. Mercury Telluride Quantum Dot Based Phototransistor Enabling High-Sensitivity Room-Temperature Photodetection at 2000 Nm. *ACS Nano* **2017**, *11* (6), 5614–5622.
- (3) Jagtap, A.; Goubet, N.; Livache, C.; Chu, A.; Martinez, B.; Gréboval, C.; Qu, J.; Dandeu, E.; Becerra, L.; Witkowski, N.; et al. Short Wave Infrared Devices Based on HgTe Nanocrystals with Air Stable Performances. *J. Phys. Chem. C* **2018**, *122* (26), 14979–14985.
- (4) Jagtap, A.; Martinez, B.; Goubet, N.; Chu, A.; Livache, C.; Gréboval, C.; Ramade, J.; Amelot, D.; Troussset, P.; Triboulin, A.; et al. Design of a Unipolar Barrier for a Nanocrystal-Based Short-Wave Infrared Photodiode. *ACS Photonics* **2018**, *5* (11), 4569–4576.
- (5) Tang, X.; Ackerman, M. M.; Guyot-Sionnest, P. Thermal Imaging with Plasmon Resonance Enhanced HgTe Colloidal Quantum Dot Photovoltaic Devices. *ACS Nano* **2018**, *12* (7), 7362–7370.
- (6) Ackerman, M. M.; Tang, X.; Guyot-Sionnest, P. Fast and Sensitive Colloidal Quantum Dot Mid-Wave Infrared Photodetectors. *ACS Nano* **2018**, *12* (7), 7264–7271.
- (7) Geiregat, P.; Houtepen, A. J.; Sagar, L. K.; Infante, I.; Zapata, F.; Grigel, V.; Allan, G.; Delerue, C.; Van Thourhout, D.; Hens, Z. Continuous-Wave Infrared Optical Gain and Amplified Spontaneous Emission at Ultralow Threshold by Colloidal HgTe Quantum Dots. *Nat. Mater.* **2018**, *17* (1), 35–42.
- (8) Al-Otaify, A.; Kershaw, S. V.; Gupta, S.; Rogach, A. L.; Allan, G.; Delerue, C.; Binks, D. J. Multiple Exciton Generation and Ultrafast Exciton Dynamics in HgTe Colloidal Quantum Dots. *Phys. Chem. Chem. Phys.* **2013**, *15* (39), 16864–16873.
- (9) Livache, C.; Goubet, N.; Martinez, B.; Jagtap, A.; Qu, J.; Ithurria, S.; Silly, M. G.; Dubertret, B.; Lhuillier, E. Band Edge Dynamics and Multiexciton Generation in Narrow Band Gap HgTe Nanocrystals. *ACS Appl. Mater. Interfaces* **2018**, *10* (14), 11880–11887.
- (10) Beugeling, W.; Kalesaki, E.; Delerue, C.; Niquet, Y.-M.; Vanmaekelbergh, D.; Smith, C. M. Topological States in Multi-Orbital HgTe Honeycomb Lattices. *Nat. Commun.* **2015**, *6*, 6316.
- (11) Man, P.; Pan, D. S. Infrared Absorption in HgTe. *Phys. Rev. B* **1991**, *44* (16), 8745–8758.
- (12) Lhuillier, E.; Scarafagio, M.; Hease, P.; Nadal, B.; Aubin, H.; Xu, X. Z.; Lequeux, N.; Patriarche, G.; Ithurria, S.; Dubertret, B. Infrared Photodetection Based on Colloidal Quantum-Dot Films with High Mobility and Optical Absorption up to THz. *Nano Lett.* **2016**, *16* (2), 1282–1286.
- (13) Deng, Z.; Jeong, K. S.; Guyot-Sionnest, P. Colloidal Quantum Dots Intraband Photodetectors. *ACS Nano* **2014**, *8* (11), 11707–11714.
- (14) Wang, H.; Lhuillier, E.; Yu, Q.; Zimmers, A.; Dubertret, B.; Ulysse, C.; Aubin, H. Transport in a Single Self-Doped Nanocrystal. *ACS Nano* **2017**, *11* (2), 1222–1229.
- (15) Lhuillier, E.; Keuleyan, S.; Guyot-Sionnest, P. Optical Properties of HgTe Colloidal Quantum Dots. *Nanotechnology* **2012**, *23* (17), 175705.
- (16) Allan, G.; Delerue, C. Tight-Binding Calculations of the Optical Properties of HgTe Nanocrystals. *Phys. Rev. B* **2012**, *86* (16), 165437.
- (17) Kim, J.; Choi, D.; Jeong, K. S. Self-Doped Colloidal Semiconductor Nanocrystals with Intraband Transitions in Steady State. *Chem. Commun.* **2018**, *54* (61), 8435–8445.
- (18) Jagtap, A.; Livache, C.; Martinez, B.; Qu, J.; Chu, A.; Gréboval, C.; Goubet, N.; Lhuillier, E. Emergence of Intraband Transitions in Colloidal Nanocrystals. *Opt. Mater. Express* **2018**, *8* (5), 1174–1183.
- (19) Hudson, M. H.; Chen, M.; Kamysbayev, V.; Janke, E. M.; Lan, X.; Allan, G.; Delerue, C.; Lee, B.; Guyot-Sionnest, P.; Talapin, D. V. Conduction Band Fine Structure in Colloidal HgTe Quantum Dots. *ACS Nano* **2018**.
- (20) Goubet, N.; Livache, C.; Martinez, B.; Xu, X. Z.; Ithurria, S.; Royer, S.; Cruguel, H.; Patriarche, G.; Ouerghi, A.; Silly, M.; et al. Wave-Function Engineering in HgSe/HgTe Colloidal Heterostructures To Enhance Mid-Infrared Photoconductive Properties. *Nano Lett.* **2018**, *18* (7), 4590–4597.
- (21) Robin, A.; Livache, C.; Ithurria, S.; Lacaze, E.; Dubertret, B.; Lhuillier, E. Surface Control of Doping in Self-Doped Nanocrystals. *ACS Appl. Mater. Interfaces* **2016**, *8* (40), 27122–27128.

- (22) Martinez, B.; Livache, C.; Notemgnou Mouafo, L. D.; Goubet, N.; Keuleyan, S.; Cruguel, H.; Ithurria, S.; Aubin, H.; Ouerghi, A.; Doudin, B.; et al. HgSe Self-Doped Nanocrystals as a Platform to Investigate the Effects of Vanishing Confinement. *ACS Appl. Mater. Interfaces* **2017**, *9* (41), 36173–36180.
- (23) Chen, M.; Guyot-Sionnest, P. Reversible Electrochemistry of Mercury Chalcogenide Colloidal Quantum Dot Films. *ACS Nano* **2017**, *11* (4), 4165–4173.
- (24) Martinez, B.; Livache, C.; Meriggio, E.; Xu, X. Z.; Cruguel, H.; Lacaze, E.; Proust, A.; Ithurria, S.; Silly, M. G.; Cabailh, G.; et al. Polyoxometalate as Control Agent for the Doping in HgSe Self-Doped Nanocrystals. *J. Phys. Chem. C* **2018**, *122* (46), 26680–26685.
- (25) Katsuki, S.; Kunimune, M. Effect of Pressure on the Band Structure of HgTe: Pseudopotential Calculation. *J. Phys. Soc. Jpn.* **1971**, *31* (2), 337–341.
- (26) Huang, T.; Ruoff, A. L. Pressure-Induced Phase Transitions of HgSe. *Phys. Rev. B* **1983**, *27* (12), 7811–7812.
- (27) Leubner, P. Strain-Engineering of the Topological Insulator HgTe, Julius-Maximilians-Universität: Würzburg, 2016.
- (28) Kirtschig, F.; van den Brink, J.; Ortix, C. Surface-State Spin Textures in Strained Bulk HgTe: Strain-Induced Topological Phase Transitions. *Phys. Rev. B* **2016**, *94* (23), 235437.
- (29) Brüne, C.; Liu, C. X.; Novik, E. G.; Hankiewicz, E. M.; Buhmann, H.; Chen, Y. L.; Qi, X. L.; Shen, Z. X.; Zhang, S. C.; Molenkamp, L. W. Quantum Hall Effect from the Topological Surface States of Strained Bulk HgTe. *Phys. Rev. Lett.* **2011**, *106* (12), 126803.
- (30) San-Miguel, A.; Wright, N. G.; McMahon, M. I.; Nemes, R. J. Pressure Evolution of the Cinnabar Phase of HgTe. *Phys. Rev. B Condens. Matter* **1995**, *51* (14), 8731–8736.
- (31) Wright, N. G.; McMahon, M. I.; Nemes, R. J.; San-Miguel, A. Crystal Structure of the Cinnabar Phase of HgTe. *Phys. Rev. B* **1993**, *48* (17), 13111–13114.
- (32) Werner, A.; Hochheimer, H. D.; Strössner, K.; Jayaraman, A. High-Pressure x-Ray Diffraction Studies on HgTe and HgS to 20 GPa. *Phys. Rev. B* **1983**, *28*, 3330–3334.
- (33) McMahon, M. I.; Wright, N. G.; Allan, D. R.; Nemes, R. J. High-Pressure Crystal Structure of HgTe-IV. *Phys. Rev. B Condens. Matter* **1996**, *53* (5), 2163–2166.
- (34) Kafalas, J. A.; Gatos, H. C.; Lavine, M. C.; Banus, M. D. High Pressure Phase Transition in Mercury Selenide. *J. Phys. Chem. Solids* **1962**, *23* (11), 1541–1544.
- (35) Keuleyan, S.; Lhuillier, E.; Guyot-Sionnest, P. Synthesis of Colloidal HgTe Quantum Dots for Narrow Mid-IR Emission and Detection. *J. Am. Chem. Soc.* **2011**, *133* (41), 16422–16424.
- (36) Jiang, J. Z. Phase Transformation in Nanocrystals under Pressure. *Defect Diffus. Forum* **2002**, *208–209*, 175–186.
- (37) Tolbert, S. H.; Alivisatos, A. P. Size Dependence of a First Order Solid-Solid Phase Transition: The Wurtzite to Rock Salt Transformation in CdSe Nanocrystals. *Science* **1994**, *265* (5170), 373–376.
- (38) Düz, I.; Erdem, I.; Ozdemir Kart, S.; Kuzucu, V. First Principles Investigations of HgX (X=S, Se and Te). *Arch. Mater. Sci. Eng.* **2016**, Vol. 79 (nr 1).
- (39) Kurilo, I. V.; Alekhin, V. P.; Rudyi, I. O.; Bulychev, S. I.; Osypyshin, L. I. Mechanical Properties of ZnTe, CdTe, CdHgTe and HgTe Crystals from Micromechanical Investigation. *Phys. Status Solidi A* **1997**, *163* (1), 47–58.
- (40) Jacobs, K.; Wickham, J.; Alivisatos, A. P. Threshold Size for Ambient Metastability of Rocksalt CdSe Nanocrystals. *J. Phys. Chem. B* **2002**, *106* (15), 3759–3762.
- (41) Jacobs, K.; Zaziski, D.; Scher, E. C.; Herhold, A. B.; Alivisatos, A. P. Activation Volumes for Solid-Solid Transformations in Nanocrystals. *Science* **2001**, *293* (5536), 1803–1806.
- (42) Xiao, G.; Wang, Y.; Han, D.; Li, K.; Feng, X.; Lv, P.; Wang, K.; Liu, L.; Redfern, S. A. T.; Zou, B. Pressure-Induced Large Emission Enhancements of Cadmium Selenide Nanocrystals. *J. Am. Chem. Soc.* **2018**, *140* (42), 13970–13975.
- (43) Saini, P. K.; Singh, D.; Ahlawat, D. S. Calculations of Electronic Band Structure and Optical Properties of HgTe under Pressure. *Indian J. Pure Appl. Phys. IJPAP* **2017**, *55* (9), 649–654.
- (44) Latussek, V.; Becker, C. R.; Landwehr, G.; Bini, R.; Ulivi, L. Deformation Potentials of the Semimetal HgTe. *Phys. Rev. B* **2005**, *71* (12), 125305.
- (45) Svane, A.; Christensen, N. E.; Cardona, M.; Chantis, A. N.; van Schilfgaarde, M.; Kotani, T. Quasiparticle Band Structures of beta-HgS, HgSe, and HgTe. *Phys. Rev. B* **2011**, *84* (20), 205205.
- (46) Ithurria, S.; Guyot-Sionnest, P.; Mahler, B.; Dubertret, B. Mn<sup>2+</sup> as a Radial Pressure Gauge in Colloidal Core/Shell Nanocrystals. *Phys. Rev. Lett.* **2007**, *99* (26), 265501.
- (47) Deligoz, E.; Colakoglu, K.; Ciftci, Y. Elastic, Electronic, and Lattice Dynamical Properties of CdS, CdSe, and CdTe. *Phys. B Condens. Matter* **2006**, *373* (1), 124–130.



TOC graphic

